Deployable 3D architectures from wafer-fabricated precursors

Yue Wang[1], Kelvin Shum[1], Yuyang Song[2], and Tian Chen[1,3*]

[1]Department of Mechanical & Aerospace Engineering, University of Houston
[2]Toyota Research Institute of North America
[3]Department of Aeronautics, Imperial College London
[*]Corresponding author: tian.chen@imperial.ac.uk

We demonstrate that standard wafer fabrication can produce free-standing, mechanically stable, doubly-curved 3D structures with prescribed Gaussian curvature — a capability not previously achieved through semiconductor manufacturing. The stability of the deployed structures is realized through the bistable nature of their constituent auxetic unit cells. To impose prescribed Gaussian curvatures through deployment, we conformally flatten the target 3D mesh onto the 2D plane and locally tune the microstructure of each unit cell such that its second stable equilibrium occurs at the required isotropic expansion. The resulting precursor features a spatially heterogeneous tessellation. This generative method is validated on a spherical cap deployed from a flat disk through indentation, with deployment accuracy and structural stability confirmed numerically and experimentally. The method is further applied to a range of complex 3D shapes with both positive and negative curvatures. As a functional demonstration, paraboloidal reflectors with tunable focal lengths are fabricated and deployed, with reflected patterns agreeing with geometric optics predictions. This work paves the way from flexible electronics towards deployable electronics, broadening the spectrum of realizable 3D semiconductor devices.

Introduction

Three-dimensional mesoscale structures with doubly-curved geometries promise to transform medical engineering, curved electronics, and wireless communication [1–3]. Current efforts to realize three-dimensional electronic and photonic systems follow two distinct fabrication paradigms: direct three-dimensional microfabrication and planar wafer fabrication followed by transformation or assembly into three-dimensional forms [4–6]. Recent advances in multiphoton lithography (MPL), including two-photon polymerization, have significantly expanded the capabilities of the former, enabling freeform 3D architectures, writing on non-planar substrates, and a range of hybrid and transfer-based integration strategies [7–10].

With the shared long-term goal of digital electronics in 3D, MPL advances this objective by offering geometric freedom and localized material patterning through serial, voxel-by-voxel writing [11]. This serial nature, together with the reliance on material-specific photoresists and sequential processing steps, represents a fundamental distinction from wafer-scale fabrication and can pose challenges for large-area scalability, throughput, and heterogeneous integration within established semiconductor workflows [12, 13].

Here we ask: can standard planar wafer fabrication be used to manufacture precursors that deploy uniquely, stably, and accurately to prescribed doubly-curved 3D geometries without a supporting substrate? We address this question by combining conformal mapping, bistable auxetic microstructure design, and multi-step lithography into a unified fabrication and deployment pipeline. This approach leverages existing pla-

nar wafer fabrication, where parallel processing, yield, and heterogeneous material integration are already mature, and combines it with mechanically programmed, bistable deployment to achieve prescribed three-dimensional architectures. We treat the 2D-to-3D deployment as an integral step of the manufacturing process: the planar precursor fabricated on the wafer is an intermediate product, and the deployed 3D structure is the final manufactured device [14–16].

To achieve this, we address three fundamental challenges related to 1) accommodating the necessary mechanical stretch, 2) targeting specific 3D shapes, and 3) ensuring structural stability. First, Gauss's Remarkable Theorem dictates that in-plane stretch and/or contraction is required to alter the Gaussian curvature of a surface [17]. To achieve significant curvature change, the necessary stretch often exceeds the rupture limits of thin film substrates [18,19]. To overcome this, one may constrain the designs to isometric deformations or bending [5,14,20,21]. Alternatively, a microstructural approach such as Kirigami, serpentine, or origami patterns may be adopted to accommodate a larger effective stretch of the overall material [22–27].

Second, current techniques generally do not allow target geometries to be prescribed *a priori*. By virtue of periodic patterning, most 2D precursor designs are inherently 3D-shape-agnostic, *i.e.*, they may equally conform to many different substrate geometries. As a corollary, it is also unknown *a priori* whether the required stretch of a specific contour exceeds the allowable stretch of the precursor, thereby causing tear and/or wrinkling [5,14,28]. Instead, we construct a conformal map of the target 3D design and generate a spatially varying 2D pattern accordingly. This 2D pattern can only deploy to that specific 3D shape, up to isometry.

Third, the mechanical stability of flexible electronics in the absence of a substrate remains undefined [16,29–32], *e.g.*, when the substrate is removed, most flexible electronics will collapse back to 2D. Mechanical bistability may address this challenge [33–35], yet this has been rarely adopted on a meso- or micro-scale. Here, by engineering a second stable state in the target 3D design, we can imbue mechanical stability to 3D mesoscale structures after shape deployment [34–36].

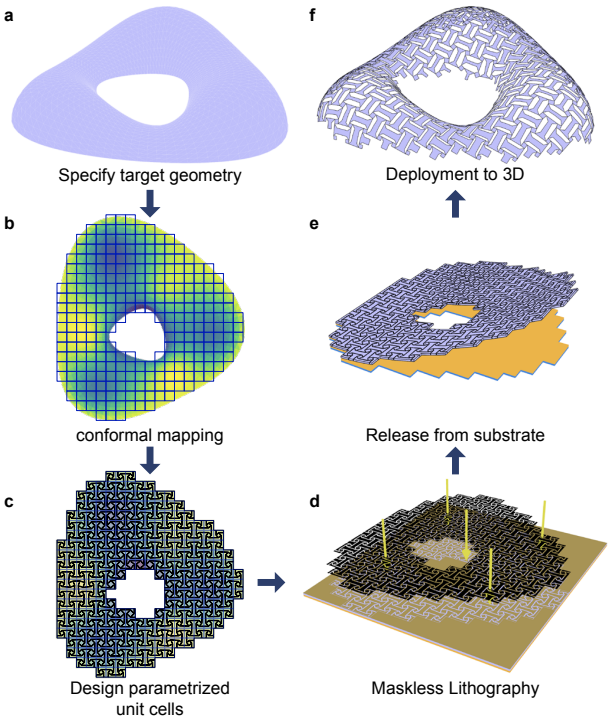

Figure 1: **Pipeline for the manufacturing of deployable 3D mesoscale structures.** a) A target 3D geometry is specified as a surface mesh. We use the example of an annulus with both positive and negative Gaussian curvature. b) The mesh is conformally flattened to the 2D plane; the color spectrum indicates the local isotropic expansion factor λ per mesh face, and a regular square grid is superimposed. c) The geometric parameters of each unit cell are tuned so that its second stable equilibrium occurs at the required local expansion λ. This yields a spatially heterogeneous 2D precursor pattern. d) The precursor pattern is transferred to a polyimide film via maskless lithography and reactive-ion etching. e) The patterned film is mechanically released from the wafer substrate. f) The free-standing precursor is deployed through mechanical indentation into the prescribed 3D geometry, where it is stabilized by the bistable nature of its constituent unit cells.

While target shape morphing through con-

formal mapping has been utilized in the literature [37, 38], including by the authors [34, 39], the central result of this work is that free-standing, mechanically stable, doubly-curved 3D structures with prescribed Gaussian curvature can be produced from standard wafer fabrication. We treat the 2D-to-3D deployment as an integral step of the manufacturing process: the planar precursor fabricated on the wafer is an intermediate product, and the deployed 3D structure is the final manufactured device. We show 1) that masked lithography can fabricate bistable auxetic precursor structures with spatially heterogeneous aperiodic patterns algorithmically designed to target specific 3D shapes, 2) that these wafer-fabricated precursors can be released from the substrate and mechanically deployed uniquely and stably to the target 3D geometry without a supporting substrate, and 3) that the resulting free-standing 3D structures are mechanically stable and geometrically accurate, as confirmed through numerical simulation and experiment. This integration of target shape deployment and generalizable semiconductor processing paves the way for a new class of devices including miniature antennas, conformal sensor arrays, micro-optical components, and human-interfacing medical implants [30, 31, 40].

Results

Design & fabrication pipeline

We demonstrate a protocol that utilizes wafer fabrication to manufacture a 2D precursor, which is then deployed into a free-standing doubly curved 3D structure. Using an annulus geometry with both positive and negative Gaussian curvature as an example (Fig. 1a), the protocol first specifies a 3D surface mesh of the target geometry. A discrete conformal map is then computed [41] to flatten this mesh onto the 2D plane, resulting in a 2D mesh with identical connectivity (Fig. 1b). The vertices are optimized to minimize angular distortion of the triangular mesh faces; this necessarily requires the area of each triangle to isotropically scale, as indicated by the expansion factor λ. A grid of squares of edge length L is superimposed onto the flattened mesh, and each square is assigned the local λ value from the mesh faces underneath. This areal scaling is mechanically enabled using a parametric unit cell that exhibits auxeticity and bistability with a tunable second equilibrium strain, $\varepsilon_{\text{equil}}$. By setting $\varepsilon_{\text{equil}} = \lambda - 1$ per unit cell, the geometric parameters of each unit cell are determined, yielding a spatially heterogeneous 2D precursor pattern (Fig. 1c). The precursor is fabricated through a multi-step lithography process using polyimide PI 2611 (HD Microsystems Inc.) (Fig. 1d), released from the wafer substrate (Fig. 1e), and mechanically deployed into the prescribed 3D geometry, where it is stabilized by the bistable nature of its constituent unit cells (Fig. 1f).

Mechanics of unit cell microstructure

First, we analyze the kinematics and mechanics of the unit cell microstructure that enables auxeticity and bistability. All deployable surfaces in this work are tessellated with unit cells of the same initial edge length $L = 220\,\mu\text{m}$ (Fig. 2a). The microstructure of this rotating square auxetic pattern consists of a series of slits. These are defined by the side length of l and a tilting angle θ. The slits have a width of s, and they form four inner squares connected to the outer geometries with hinges of width c. The detailed geometric definition is found in SI Sec. 2.1. This design is chosen because it simultaneously satisfies three properties required by the conformal deployment framework: (1) a Poisson's ratio of $\nu = -1$ between the rest and second equilibrium state, (2) mechanical bistability with a tunable second equilibrium strain through the rotating square inclination θ and edge length l, and (3) isotropic expansion over the entire strain range [26, 35, 42, 43]. Isotropic expansion is critical because conformal maps prescribe a purely isotropic areal scaling λ at each point; a unit cell that expands anisotropically would introduce shear distortion incompatible with this framework.

When this unit cell undergoes uniaxial tension, the squares counter-rotate by an angle ϕ from

0 to 2θ to accommodate the stretch. Kinematically, this results in an isotropic expansion of the unit cell from the initial edge length L to λL [34] where $\lambda_{\text{kinematic}} = 1 + 2l\sin\theta$ assuming $c, s = 0$. Note that at all intermediate values of ϕ, kinematic incompatibility must be resolved through deformation. As a result, two stable equilibria exist at $\phi = 0$ and 2θ.

We leverage wafer fabrication to manufacture all specimens in this manuscript. To facilitate experiment characterization of unit cells at the micron-scale, we fabricate 8 by 8 periodic tessellations of the different parametric variations. As shown in Fig. 2b, first, (i) the wafer is coated with (A) a silane coupling agent (3-Aminopropyl)triethoxysilane (APTES), (B,C) two layers of polyimide (PI-2611, 6 µm), and (D) a photoresist (AZ 12XT-20PL, 11 µm), (ii) then maskless photolithography is used to pattern the microstructure onto the photoresist, (iii) the sample is then uniformly etched until the depth of the slit on the top layer of PI is reduced by 75% using Reactive-ion etching (RIE). It is not etched through to minimize stress concentration during the peeling process that follows. In (iv), the upper layer of PI is mechanically peeled from the bottom, and (v) subjected to secondary etching until the slits are fully formed. (vi) Lastly, the sample is immersed in acetone to dissolve the remaining photoresist. Compared to widely used microfabrication approaches, such as employing sacrificial layers [32, 44], our protocol leverages the low surface adhesion between two polyimide layers to detach sample from substrate while minimizing stress concentrations. To evaluate the repeatability of the fabrication method, we measure the thickness of the polyimide film ($6.08 \pm 0.66\,\mu$m) and of the photoresist ($12.41 \pm 0.16\,\mu$m) in the thickness direction. In-plane, we compare the designed versus fabricated feature sizes of the critical slit and hinge dimensions. See SI Sec. 4.1 for details.

A micro-mechanical stage is constructed to apply tension to the 8 by 8 periodic tessellations, which is designed to expand to a prescribed stretch in-plane (See SI Sec. 5.1). The experiment is conducted under an optical microscope to measure the effective stretch. The boundary cells are connected with angled beams (Fig. 2c) which are designed to allow free expansion in the orthogonal direction, *i.e.*, at the second equilibrium, the beams become parallel. From all combinations of l and θ, two extremes of the λ spectrum are experimentally tensioned to 1.2 times their respective second equilibria and relaxed. The resulting effective-stress and stretch curves show an initial stiffening followed by softening until the stretch equals to λ where the behavior rapidly stiffens again (Fig. 2d). The initial behavior is attributed to the partial opening of all unit cells as expected from linear elasticity. The softening is a result of the column by column triggering of bistability (Fig. 2e, see Video 1). Due to the imperfections in fabrication and the boundary conditions, the triggering force per column differ minutely. This causes some columns of unit cells to snap prior to others. At the expected λ, all unit cells are in their second equilibria, and further tensioning results in a significantly stiffer response. During unloading at the second equilibria, the reaction forces reach zero as indicative of static equilibrium. Further unloading results in out-of-plane buckling with negligible reaction forces.

Next, we quantify the mechanical response of all combinations of the two geometric parameters θ and l using Finite Element (FE) analyses. We identify a range of feasible θ from 0.1π to 0.28π, l from $0.1L$ to $0.4L/(\sin\theta + \cos\theta)$, and set the increments at 0.01π and $0.01L$ respectively. Each unit cell microstructure is meshed using quadratic shell elements. Periodic boundary conditions are imposed on the four edges, and a stretch is prescribed from 1 to $1.2\lambda_{\text{kinematic}}$. The material behavior of polyimide is detailed in SI Sec. 1. The detailed FE protocol is outlined in Methods and SI Sec. 3.1. The resulting stress-strain relationships inform the bistability of the different unit cells as well as the stretch at their second equilibria λ (if any). Of the parametric combinations of θ and l that result in a bistable microstructure as defined by the presence of a second local minimum in the strain energy, we identify the permissible spectrum of λ as between $[1.2, 1.6]$.

With the parametric sweep, we construct a li-

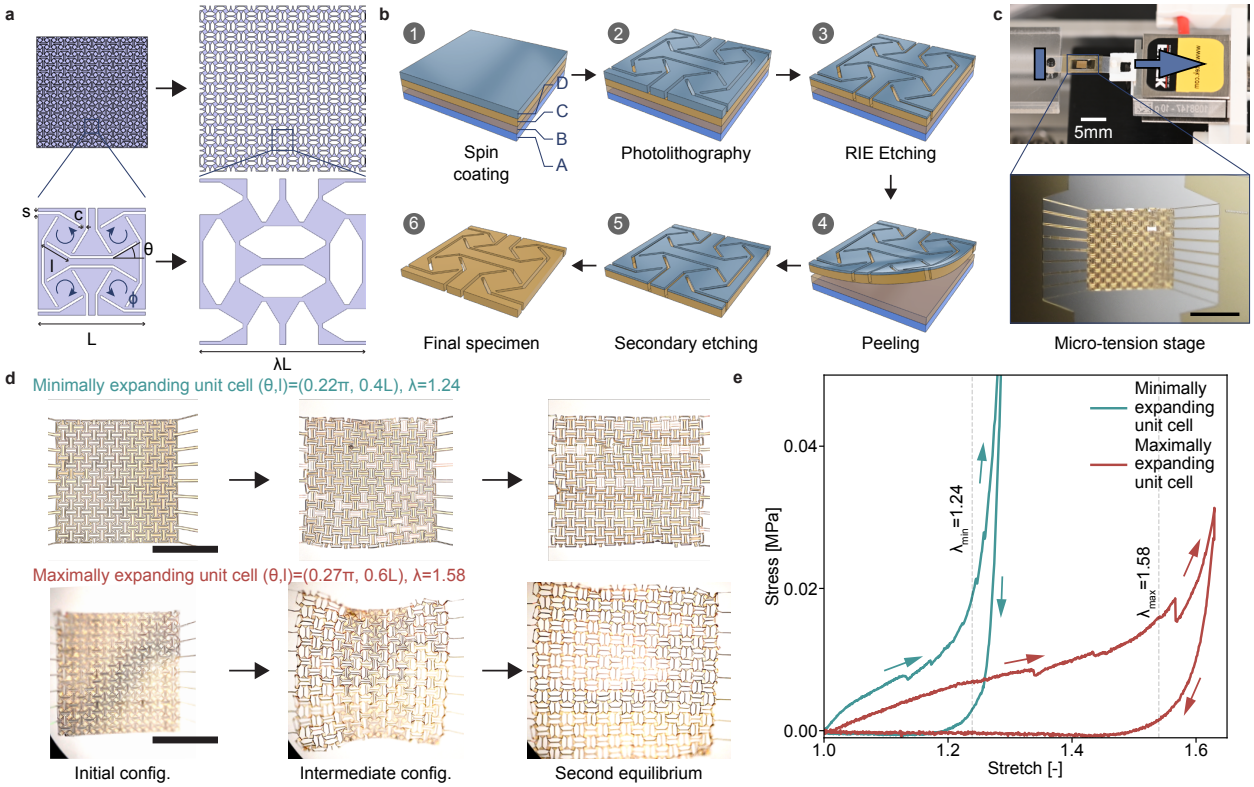

Figure 2: **Mechanics of bistable auxetic unit cells.** a) Each 2D pattern is tessellated using a grid of unit cells. The microstructure of each unit cell features a number of slits. As the unit cells stretch, the inner squares counter-rotate. By changing internal geometric parameters l and θ, the stretch at the second equilibrium λ can be tuned. b) Wafer fabrication protocol used by all specimens in this work featuring multiple masking and etching steps. The structure is physically peeled from the substrate prior to deployment. c) Micro-tensile experimental setup featuring an 8x8 tessellation, The lower scale bar is 1 mm. d) From all combinations of l and θ, two extremes of the λ spectrum are tension tested. The Microscopic image sequence of the deformations of these are shown. e) The stress-strain curves of the two unit cells respectively. The vertical dashed lines indicate the strains at the second equilibria.

brary of unit cells that feature the correspondence between the stretch at the second equilibrium λ and the input geometric parameters θ and l. Further, we identify the range of λ values that will result physically realizable microstructures that exhibit bistability. By examining the internal stresses, we validate that the hinges experience negligible plasticity. See SI Sec. 3.2 for the results of all parametric combinations.

Generative algorithm

Now, we discuss an algorithmic approach to design a spatially heterogeneous 2D tessellation that deploys to a prescribed 3D shape when all of its unit cells reach their respective second equilibrium. We observe that all unit cells in the design space expand isotropically up to their respective second equilibrium with a stretch equaling to λ. This leads us to use conformal mapping to calculate the necessary scalar field of λ as a function of the prescribed 3D shape. Once λ is calculated per coordinate on the 2D mesh, the values are then further translated to the unit cell geometric parameters θ and l using the unit cell library computed previously.

A conformal map is a function that locally preserves angles but not areas. Mechanically, this

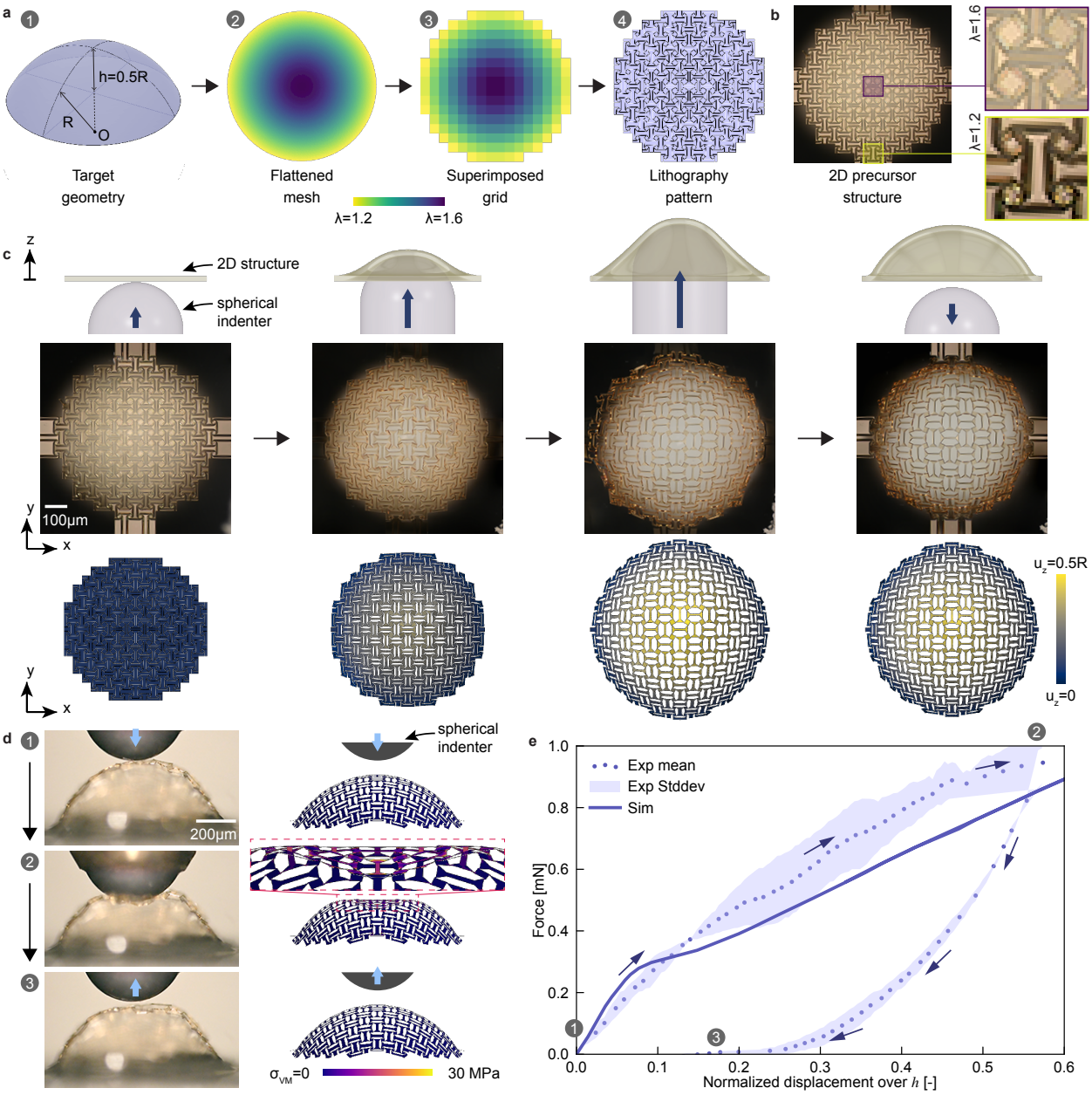

Figure 3: **Design, fabrication and mechanical behavior of a deployable 3D spherical dome.** a) Digital geometric processing that translates a target 3D mesh to a lithography mask by first conformal mapping to the 2D plane, grid sampling the scale factor λ, and then selecting the geometric parameters per unit cell. b) Wafer fabrication of the 2D spatially heterogeneous precursor showing unit cells of different λ. c) 2D to 3D deployment using a mechanical indenter. This deployment step is part of fabrication process that yields the 3D structure. d) Mechanical indentation test to demonstrate the stability of the 3D structure after deployment. e) Experimental and simulation results of mechanical indentation. See SI Video 2.

implies each material point may expand or contract but not distort in shape, which our unit cells satisfy. Thereby, if we abstract the prescribed 3D design by its Gaussian curvature K, we can simply relate K directly to the Laplace

of the scalar field λ (Eq. 1),

$$K = \Delta_f \log \lambda, \tag{1}$$

where, Δ_f is the Laplace-Beltrami operator [28, 45].

Mechanistically speaking, the spatially varying degree of stretch on a surface will cause geometric frustration that "pop" the surface out into 3D [46]. This occurs when out-of-plane bending becomes more energetically favorable as compared to in-plane compression of the constituent material. Indeed, shape morphing that explicitly leverage this principle have been demonstrated [47–49].

To outline the algorithm, we target the deployment from a disk to a quarter-spherical dome, $h = 0.5R, R = 1.35\,\text{mm}$ (Fig. 3a,i). First, we algorithmically generate the 2D precursor, which features a spatially heterogeneous unit cell tessellation. While stereographic projection may be used to calculate a continuous λ field for such a canonical geometry [50] (see SI Sec. 2.2), we use Boundary First Flattening (BFF) [41] for generality in processing arbitrary discrete geometries (see SI Sec. 2.3). BFF computes conformal maps of input meshes by minimizing angular distortion while flattening from 3D to 2D. The local scale factor λ at each mesh face is computed as the areal change of each pair of corresponding mesh faces, *i.e.*, $\lambda = \sqrt{A_{3D}/A_{2D}}$, where A_{3D} and A_{2D} are the areas of the corresponding mesh faces in 3D and 2D respectively (Fig. 3a,ii).

Next, a grid of squares of edge length L is overlaid on the conformally flattened 2D mesh. By inferring the λ of each square from the mesh faces underneath, we calculate the necessary θ and l of the unit cell microstructure to slot in the square (Fig. 3a,iii,iv). Should the λ resulting from BFF exceed the bounds of the permissible λ spectrum from the unit cell analysis, then no combinations of θ and l can satisfy the required scaling, and the target geometry cannot be deployed to with this particular microstructure without injecting singularities [51].

The wafer fabrication protocol outlined in Fig. 2d is used to fabricate all 2D precursor patterns (Fig. 3b). For deployment, a spherical indenter ($r_{\text{indenter}} = 0.4\,\text{mm}$) is used. The 2D pattern is fixed at the midpoint of the four edges. The indenter connected to a linear translation stage pushes up against the pattern until the vertical displacement reaches $d = 1.2h$. This is larger than the height of the dome to ensure each unit cell is stretched beyond their respective second equilibrium (Fig. 3c). The indenter is then retracted to show that the dome similarly retracts briefly until the intended height is reached, then detaches from the indenter.

To assess the repeatability of the deployment process, three dome structures are fabricated and deployed following the same procedure. The measured dome heights are $0.671(18)\,\text{mm}$ and lateral spans are $2.29(13)\,\text{mm}$ (mean $\pm$ s.d.) respectively. This confirms consistent and repeatable deployment behavior across samples. While the dome height is achieved accurately, the systematic underestimation of the span (target: $2.70\,\text{mm}$, underestimation of 15%) is attributed to the boundary conditions of the physical structure, which constrain free expansion at the edge points. To quantify geometric accuracy, a 3D surface reconstruction of a representative deployed dome is generated using focal-plane stacking (see SI Sec. 6). The pointwise geometric deviation between the reconstructed surface and the target hemisphere is mapped in SI Fig. 12, confirming that deviations are concentrated at the rim ($\delta \leq 0.14R$), with the central region closely matching the target geometry. For further validation, to show that the 3D structure is not shaped as a result of indentation, we fabricate a periodic tessellation of unit cells following the same 2D outline. Following the identical deployment process, the structure becomes wrinkled and does not approximate a hemisphere (See SI Sec. 5.4).

Using shell elements and static analysis, the FE simulation of deployment artificially expands the distance between every pair of neighboring unit cells from L to their respective λL where the λ of each pair is averaged. The total strain energy shows two local minima during the simulation, demonstrating the stability of the deployed 3D structure (see SI Sec. 3.3). This method of simulated deployment can be universally applied

as the target 3D design is not supplied *a priori*. By not applying displacements at the boundary nodes, this method circumvents the instabilities inherent in each unit cell. We find the resulting deployed 3D structure matches closely to the experimental counterpart with the simulated dome height being 0.71 mm. See Methods for details of the FE setup.

Lastly, to demonstrate structural stability, the indenter is flipped to press downward onto the deployed dome as it rests against a flat surface. The displacement of the indenter is increased until $d = 0.6h$ upon which it reverses. Microscopic imaging of the deformation shows a behavior similar to those of continuum shells where a localized indent forms [52]. We note that the dome does not fully recover its original shape after significant indentation (Fig. 3d). This partial irreversibility is attributed to localized damage in the hinge regions of the unit-cell microstructure under off-path loading conditions. Specifically, indentation introduces localized bending and compressive stresses that are absent during deployment, leading to plastic yielding and buckling of hinge elements. Importantly, this behavior does not originate from the deployment process itself, which follows a prescribed deformation pathway to the second stable equilibrium.

The FE counterpart replicates the experimental setup and allows access to the internal stress state of the dome. The force-displacement behavior of the simulation matches well with that of the experiment for the loading portion (Fig. 3e). As the simulation model does not account for frictional dissipation (of the dome against the flat surface), the unloading is not predicted.

Deployment of complex designs

To demonstrate the versatility of the 2D to 3D deployment methodology, we specify a number of target shapes with different topology and geometry (Fig. 4). These include: the cornea geometry shown in detail in SI Sec. 7, a double dome with a negative curvature region in between [34], a threefold rotational symmetric shape with open boundaries that are elevated [34], the top of the Lilium tower [53], and an annulus shown in Fig. 1 [54]. The Euler characteristic of shapes 3 and 5 are 0, whereas the others are 1 [55]. In each case, the 2D precursors are fabricated in the 2D state with some boundary units connected to the substrate. The five shapes are designed using 1126, 667, 501, 590, 515 unit cells respectively. Upon mechanical deployment through indentation, the 3D structures faithfully reproduce the target input geometries (See SI Video 3). Note that not only is the global shape predictable, the spatial coordinates and connectivity of each unit cell can be inherently inferred. This allows an array of sensors to be precisely placed.

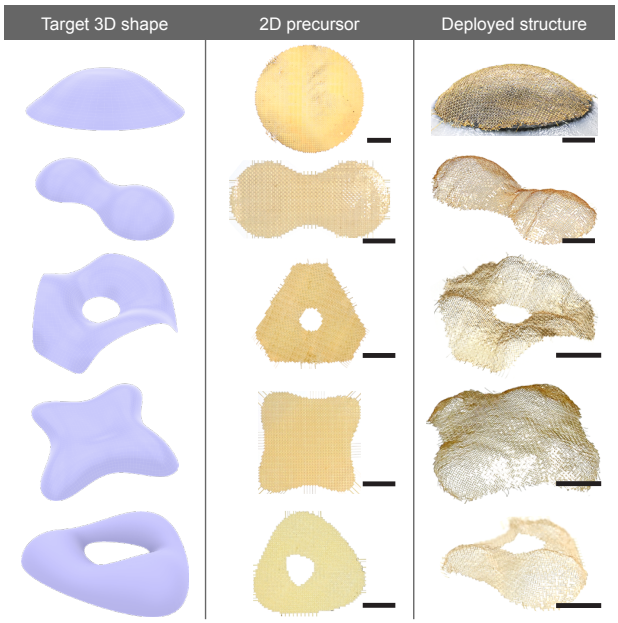

Figure 4: **Experimental demonstration of complex target 3D designs.** The 3D meshes are supplied to the algorithm which generates the corresponding 2D precursor lithography patterns. These are fabricated and deployed to 3D structures of prescribed shapes. Scale bars: 2 mm.

Paraboloidal reflectors

We use paraboloidal reflectors as a representative geometry to demonstrate precise control over the curvature of the deployed 3D structures. Paraboloidal geometries provide a well-defined benchmark: their optical response is highly sen-

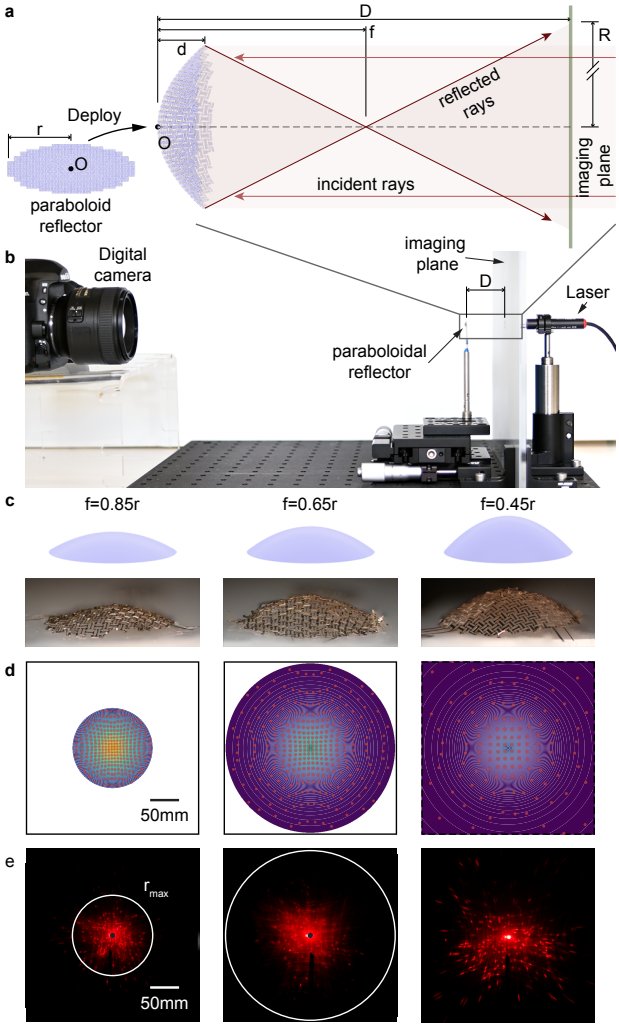

Figure 5: **Demonstration of proof-of-concept doubly-curved paraboloidal reflectors with tunable focal distances.** a) The schematic diagram of experimental setup of the paraboloidal reflector shows the incident rays reflecting off the deployed reflector, converging at a focal point before diverging towards the imaging plane. b) Photograph of the experimental setup. c) Target 3D design, and the fabricated and deployed 3D reflectors with focal lengths ranging from $f = 0.85r$, $0.65r$ to $0.45r$.d) Analytically calculated reflected pattern for the three samples at a distance $D = 40\,\text{mm}$, note that the reflected pattern of specimen $f = 0.45r$ exceeds the bounding box. e) Photography of the reflected patterns with the analytically calculated maximum radii labeled.

sitive to surface curvature deviations, and the reflection pattern under collimated illumination can be analytically predicted. Furthermore, conventional fabrication of three-dimensional reflective surfaces often relies on high-precision machining, molding, or micro-scale 3D printing [56]. In contrast, our planar wafer-based fabrication strategy offers practical advantages for device integration, since wafer fabrication readily supports multilayer processing and the incorporation of additional functional materials such as sensing or electronic components.

To demonstrate this capability, we design three deployable reflectors, each targeting a different focal length, *i.e.*, $f = 0.85r, 0.65r, 0.45r$, but all sharing the same radius $r = 3\,\text{mm}$. All three reflector designs employ the same number of bistable unit cells ($n = 79$) and the same edge length $L = 220\,\mu\text{m}$. An optical characterization experiment is constructed to demonstrate accurate reflective behavior. The planar precursor is first deployed and then positioned at a distance $D = 40\,\text{mm}$ from an imaging plane. A collimated visible laser beam of 3 mm in diameter (Thorlabs, PL202, 635 nm, 1 mW) uniformly illuminates the entire surface of the reflector. Reflected rays propagate toward and are recorded on the opposing imaging plane (Fig. 5a). The pattern on the imaging plane is captured using a digital camera placed behind (Fig. 5b).

The 2D precursors are designed and fabricated using the wafer-scale lithography protocol described above. To enhance optical reflectivity, a thin gold layer is deposited onto the polyimide precursor as a final fabrication step. After mechanical deployment, the resulting 3D structures closely approximate the target paraboloidal geometries (Fig. 5c). To predict the reflected patterns, we employ a ray-based geometric optics model using the known parameters f, r and D (Fig. 5d). First, we consider the reflector as a smooth parabolic surface, and analytically derive the intensity profile as a function of the radial distance from the center. This continuous analysis confirms that the reflected intensity decays rapidly away from the center, explaining why the experimentally measured spatial extent of the reflected light appears smaller than the

predicted geometric boundary. Recognizing that the deployed structure contains many voids, we additionally model the reflections from only the rotating squares within each bistable unit cell. Each square is assumed to be locally flat, and one ray per square is traced according to the local surface normal and projected onto the imaging plane. Each red dot in Fig. 5d therefore represents the intersection of a single reflected ray with the imaging plane. This discrete ray tracing captures the characteristic shape and spatial distribution of the reflected pattern, including the diagonal features arising from the square unit-cell architecture. As expected for paraboloidal geometries, reflected rays converge at the designed focal length before diverging toward the imaging plane (see SI Sec. 7.1 for details).

In both continuous and discrete numerical approximations, the predicted ray distributions show a strong accumulation of reflected rays near the center for all three focal lengths, with the intensity decaying rapidly outward. From the discrete ray tracing, the predicted boundary radii of the illuminated regions on the imaging plane are $R = 69.5\,\text{mm}$, $147\,\text{mm}$, and $381\,\text{mm}$ respectively. Experimentally, reflected patterns are recorded under identical illumination conditions for all samples (Fig. 5e). The measured spatial extent of the reflected light is smaller than these predicted boundaries, consistent with the rapid intensity decay confirmed by the continuous model — little measurable light reaches the geometric boundary of the pattern. For the shortest focal length case ($f = 0.45r$), the illuminated region exceeds the size of the imaging plane.

Differences between the calculated and experimental patterns arise from effects not captured in the geometric optics model, including discretization by the square unit-cell architecture, light scattering, finite surface roughness and non-uniform gold coating, partial shadowing between neighboring unit cells, and deviations of the deployed geometry from the ideal paraboloidal shape. We further note that a direct quantitative comparison of reflected intensity distributions is complicated by the fact that the discrete model accounts only for reflections from the rotating squares, whereas the fabricated reflector includes additional reflective surfaces between unit cells. The comparison is therefore intended to validate curvature control and focal behavior rather than exact point-wise intensity agreement.

Discussion

This work demonstrates that standard wafer fabrication can produce free-standing, mechanically stable, doubly-curved 3D structures with prescribed Gaussian curvature. By combining conformal mapping, bistable auxetic microstructure design, and multi-step lithography into a unified pipeline in which mechanical deployment serves as the final manufacturing step, we show that spatially heterogeneous 2D precursors can be algorithmically designed, lithographically fabricated, and mechanically deployed to target 3D geometries with accuracy confirmed both numerically and experimentally. The generality of the approach is demonstrated across a range of topologies and curvature distributions, and its geometric precision is validated through paraboloidal reflectors whose optical behavior agrees with analytical predictions. We note that the achievable curvature within a single continuous structure is bounded by the permissible range of λ of the particular microstructure design, which limits the sharpness of curvature gradients. This constraint can be addressed by stitching separately fabricated sections after deployment. Going beyond mechanical deployment, future research may investigate actuation mechanisms including magnetism [57] or pneumatic inflation [54] to enable autonomous deployment. By establishing a process-compatible pathway from planar wafer fabrication to prescribed 3D architectures, this work paves the way from flexible electronics towards *deployable electronics*, broadening the spectrum of realizable 3D semiconductor devices [2].

Methods

Material characterization

The stress-strain behavior of polyimide is obtained using a universal testing machine (Instron 68SC-2) at a displacement rate of $5\,\mathrm{mm\,s^{-1}}$. The results are shown in SI Sec. 1.

Fabrication protocol

All specimens are fabricated using the protocol outlined in Fig. 2d. The ingredients are as follows. The silane coupling agent is (3-Aminopropyl)triethoxysilane (APTES). The structural material is polyimide (PI-2611). The photoresist used is AZ 12XT-20PL. The maskless photolithography system is Bruker SF-100 Lightning. The Reactive-ion etching is performed on an Oxford Plasmalab System 100 ICP. See SI Sec. 4 for details.

Experimental setup

Mechanical tests are performed using a custom-built mesoscale testing system. The setup includes a linear motor stage (Zaber) and a force sensor (LSB200, 10 g, Futek), mounted onto the linear stage via a custom-designed 3D-printed adapter. Deformation is observed using a Nikon microscope equipped with a digital camera (Nikon D780). The entire setup is mobile and can be transported to different imaging equipment. A detailed description of the testing procedure and equipment configuration is provided in the SI Sec. 5.

Numerical Simulations

All Finite Element (FE) simulations are conducted using Abaqus static (general), accounting for geometric non-linearity. Quadratic shell elements are used to mesh all geometries in this study. The unit cell characterization is modeled with periodic boundary conditions imposed on the four edges. The deployment simulation involves establishing axial connectors between every neighboring pair of unit cells. Displacements are then assigned to each connector to locally expand each unit cell in plane. The magnitude of the displacement is calculated by the pre-calculated second equilibrium strain of the unit cells. The indentation simulation is a continuation of the deployment, and models a stiff sphere pressing down against the deployed geometry. See SI Sec. 3 for details.

Data Availability

The data that support the findings of this study are available in a GitHub repository at https://github.com/UH-AIM/deployable_wafer_architecture and will be made publicly accessible upon publication.

Code Availability

The finite element analysis scripts and image processing code used in this study are available in the same repository at https://github.com/UH-AIM/deployable_wafer_architecture and will be made publicly accessible upon publication.

References

[1] Younan Xia and George M Whitesides. Soft lithography. *Angewandte Chemie International Edition*, 37(5):550–575, 1998.

[2] John A. Rogers, Takao Someya, and Yonggang Huang. Materials and Mechanics for Stretchable Electronics. *Science*, 327(5973):1603–1607, 2010.

[3] Yuhao Liu, Matt Pharr, and Giovanni Antonio Salvatore. Lab-on-Skin: A Review of Flexible and Stretchable Electronics for Wearable Health Monitoring. *ACS Nano*, 11(10):9614–9635, 2017.

[4] Zeming Song, Xu Wang, Cheng Lv, Yonghao An, Mengbing Liang, Teng Ma, David He, Ying-Jie Zheng, Shi-Qing Huang, Hongyu Yu, et al. Kirigami-based stretchable lithium-ion batteries. *Scientific reports*, 5(1):10988, 2015.

[5] Xiaogang Guo, Xueju Wang, Dapeng Ou, Jilong Ye, Wenbo Pang, Yonggang Huang, John A. Rogers, and Yihui Zhang. Controlled mechanical assembly of complex 3D mesostructures and strain sensors by tensile buckling. *npj Flexible Electronics*, 2(1):14, 2018.

[6] Xingwang Zhang, Xiaojie Zhang, Yao Duan, Lidan Zhang, and Xingjie Ni. All-optical geometric image transformations enabled by ultrathin metasurfaces. *Nature communications*, 14(1):8374, 2023.

[7] Frank Marco den Hoed, Andrea Ottomaniello, Omar Tricinci, Luca Ceseracciu, Marco Carlotti, Patrizio Raffa, and Virgilio Mattoli. Facile handling of 3d two-photon polymerized microstructures by ultra-conformable freestanding polymeric membranes. *Advanced Functional Materials*, 33(39):2214409, 2023.

[8] Gordon Zyla and Maria Farsari. Frontiers of laser-based 3d printing: a perspective on multi-photon lithography. *Laser & Photonics Reviews*, 18(7):2301312, 2024.

[9] Gordon Zyla, Savvas Papamakarios, Dimitrios C Zografopoulos, Anna Christoforidou, George Kenanakis, Maria Farsari, and Odysseas Tsilipakos. Film-based multi-photon lithography for efficient printing of electromagnetic surface structures. *Advanced Materials Technologies*, 10(11):2402137, 2025.

[10] Joel Arriaga-Dávila, Cristian Rosero-Arias, Dirk Jonker, Margoth Córdova-Castro, Josua Zscheile, Robert Kirchner, Alan Aguirre-Soto, Robert Boyd, Israel De Leon, Han Gardeniers, et al. From single to multimaterial 3d printing of glass-ceramics for micro-optics. *Small Methods*, page 2401809, 2025.

[11] Songyun Gu, Chenkai Mao, Anna Guell Izard, Sarvesh Sadana, Dongping Terrel-Perez, Magi Mettry-Yassa, Wonjin Choi, Wenjie Zhou, Hujie Yan, Ziran Zhou, et al. 3d nanolithography with metalens arrays and spatially adaptive illumination. *Nature*, 648(8094):591–599, 2025.

[12] Satoshi Kawata, Hong-Bo Sun, Tomokazu Tanaka, and Kenji Takada. Finer features for functional microdevices. *Nature*, 412(6848):697–698, 2001.

[13] Justyna K Gansel, Michael Thiel, Michael S Rill, Manuel Decker, Klaus Bade, Volker Saile, Georg Von Freymann, Stefan Linden, and Martin Wegener. Gold helix photonic metamaterial as broadband circular polarizer. *science*, 325(5947):1513–1515, 2009.

[14] Sheng Xu, Zheng Yan, Kyung-In Jang, Wen Huang, Haoran Fu, Jeonghyun Kim, Zijun Wei, Matthew Flavin, Joselle McCracken, Renhan Wang, Adina Badea, Yuhao Liu, Dongqing Xiao, Guoyan Zhou, Jungwoo Lee, Ha Uk Chung, Huanyu Cheng, Wen Ren, Anthony Banks, Xiuling Li, Ungyu Paik, Ralph G. Nuzzo, Yonggang Huang, Yihui Zhang, and John A. Rogers. Assembly of micro/nanomaterials into complex, three-dimensional architectures by compressive buckling. *Science*, 347(6218):154–159, 2015.

[15] Gary P. T. Choi, Levi H. Dudte, and L. Mahadevan. Programming shape using kirigami tessellations. *Nature Materials*, 18(9):999–1004, 2019.

[16] Kyoseung Sim, Song Chen, Zhengwei Li, Zhoulyu Rao, Jingshen Liu, Yuntao Lu, Seonmin Jang, Faheem Ershad, Ji Chen, Jianliang Xiao, et al. Three-dimensional curvy electronics created using conformal additive stamp printing. *Nature Electronics*, 2(10):471–479, 2019.

[17] Noel J Hicks. *Notes on differential geometry*, volume 1. van Nostrand Princeton, 1965.

[18] Kenneth E Evans, MA Nkansah, IJ Hutchinson, and SC Rogers. Molecular network design. *Nature*, 353(6340):124–124, 1991.

[19] Andrew Pressley and Andrew Pressley. Gauss' theorema egregium. *Elementary differential geometry*, pages 247–268, 2010.

[20] Zihao Dong, Qipei He, Dawei Shen, Zheng Gong, Deyuan Zhang, Wenqiang Zhang, Takahito Ono, and Yonggang Jiang. Microfabrication of functional polyimide films and microstructures for flexible mems applications. *Microsystems & Nanoengineering*, 9(1):31, 2023.

[21] Zhi Liu, Xiaonan Hu, Renheng Bo, Youzhou Yang, Xu Cheng, Wenbo Pang, Qing Liu, Yuejiao Wang, Shuheng Wang, Shiwei Xu, Zhangming Shen, and Yihui Zhang. A three-dimensionally architected electronic skin mimicking human mechanosensation. *Science*, 384(6699):987–994, 2024.

[22] Vivek B Shenoy and David H Gracias. Self-folding thin-film materials: From nanopolyhedra to graphene origami. *Mrs Bulletin*, 37(9):847–854, 2012.

[23] Melina K Blees, Arthur W Barnard, Peter A Rose, Samantha P Roberts, Kathryn L McGill, Pinshane Y Huang, Alexander R Ruyack, Joshua W Kevek, Bryce Kobrin, David A Muller, et al. Graphene kirigami. *Nature*, 524(7564):204–207, 2015.

[24] Aaron Lamoureux, Kyusang Lee, Matthew Shlian, Stephen R. Forrest, and Max Shtein. Dynamic kirigami structures for integrated solar tracking. *Nature Communications*, 6(1):8092, 2015.

[25] Jie Xu, Sihong Wang, Ging-Ji Nathan Wang, Chenxin Zhu, Shaochuan Luo, Lihua Jin, Xiaodan Gu, Shucheng Chen, Vivian R Feig, John WF To, et al. Highly stretchable polymer semiconductor films through the nanoconfinement effect. *Science*, 355(6320):59–64, 2017.

[26] Lishuai Jin and Shu Yang. Engineering Kirigami Frameworks Toward Real-World Applications. *Advanced Materials*, 36(9):2308560, 2024.

[27] S M Felton, K P Becker, D M Aukes, and R J Wood. Self-folding with shape memory composites at the millimeter scale. *Journal of Micromechanics and Microengineering*, 25(8):085004, 2015.

[28] Mina Konaković, Keenan Crane, Bailin Deng, Sofien Bouaziz, Daniel Piker, and Mark Pauly. Beyond developable: Computational design and fabrication with auxetic materials. *ACM Trans. Graph.*, 35(4):89:1–89:11, 2016.

[29] Charlotte Py, Paul Reverdy, Lionel Doppler, José Bico, Benoit Roman, and Charles N Baroud. Capillary origami: spontaneous wrapping of a droplet with an elastic sheet. *Physical review letters*, 98(15):156103, 2007.

[30] Heung Cho Ko, Gunchul Shin, Shuodao Wang, Mark P. Stoykovich, Jeong Won Lee, Dong-Hun Kim, Jeong Sook Ha, Yonggang Huang, Keh-Chih Hwang, and John A. Rogers. Curvilinear Electronics Formed Using Silicon Membrane Circuits and Elastomeric Transfer Elements. *Small*, 5(23):2703–2709, 2009.

[31] Xu Cheng, Zhichao Fan, Shenglian Yao, Tianqi Jin, Zengyao Lv, Yu Lan, Renheng Bo, Yitong Chen, Fan Zhang, Zhangming Shen, Huanhuan Wan, Yonggang Huang, and Yihui Zhang. Programming 3D curved mesosurfaces using microlattice designs. *Science*, 379(6638):1225–1232, 2023.

[32] Qingkun Liu, Wei Wang, Himani Sinhmar, Itay Griniasty, Jason Z. Kim, Jacob T. Pelster, Paragkumar Chaudhari, Michael F. Reynolds, Michael C. Cao, David A. Muller, Alyssa B. Apsel, Nicholas L. Abbott, Hadas Kress-Gazit, Paul L. McEuen, and Itai Cohen. Electronically configurable microscopic metasheet robots. *Nature Materials*, 24(1):109–115, 2025.

[33] Lucy Liu, Gary P. T. Choi, and L. Mahadevan. Wallpaper group kirigami. *Proceedings of the Royal Society A: Mathe-*

matical, Physical and Engineering Sciences, 477(2252):20210161, 2021.

[34] Tian Chen, Julian Panetta, Max Schnaubelt, and Mark Pauly. Bistable auxetic surface structures. *ACM Transactions on Graphics*, 40(4):1–9, 2021.

[35] Ahmad Rafsanjani and Damiano Pasini. Bistable auxetic mechanical metamaterials inspired by ancient geometric motifs. *Extreme Mechanics Letters*, 9:291–296, 2016.

[36] Babak Haghpanah, Ladan Salari-Sharif, Peyman Pourrajab, Jonathan Hopkins, and Lorenzo Valdevit. Multistable shape-reconfigurable architected materials. *Adv. Mater*, 28(36):7915–7920, 2016.

[37] Ruslan Guseinov, Eder Miguel, and Bernd Bickel. Curveups: shaping objects from flat plates with tension-actuated curvature. *ACM Trans. Graph.*, 36(4):64–1, 2017.

[38] Mina Konaković-Luković, Julian Panetta, Keenan Crane, and Mark Pauly. Rapid deployment of curved surfaces via programmable auxetics. *ACM Transactions on Graphics (TOG)*, 37(4):1–13, 2018.

[39] Yingying Ren, Uday Kusupati, Julian Panetta, Florin Isvoranu, Davide Pellis, Tian Chen, and Mark Pauly. Umbrella meshes: elastic mechanisms for freeform shape deployment. *ACM Trans. Graph.*, 41(4):152–1, 2022.

[40] Zhoulyu Rao, Yuntao Lu, Zhengwei Li, Kyoseung Sim, Zhenqiang Ma, Jianliang Xiao, and Cunjiang Yu. Curvy, shape-adaptive imagers based on printed optoelectronic pixels with a kirigami design. *Nature Electronics*, 4(7):513–521, 2021.

[41] Rohan Sawhney and Keenan Crane. Boundary First Flattening. *ACM Trans. Graph.*, 37(1):5:1–5:14, 2017.

[42] Chuan Qiao, Filippo Agnelli, Deepak Kumar Pokkalla, Nicholas D'Ambrosio, and Damiano Pasini. Anisotropic morphing in bistable kirigami through symmetry breaking and geometric frustration. *Advanced Materials*, 36(23):2313198, 2024.

[43] Yu Lei, Yan Wang, Ruizhi Cui, Xiaolong Huang, Lei Zhang, Yuan Jin, Jinling Gao, and Biwei Deng. 3d hyperbolic kirigami metamaterials with tunable auxeticity and multistability. *Advanced Science*, 12(35):e06703, 2025.

[44] Surabhi R. Madhvapathy, Jiao-Jing Wang, Heling Wang, Manish Patel, Anthony Chang, Xin Zheng, Yonggang Huang, Zheng J. Zhang, Lorenzo Gallon, and John A. Rogers. Implantable bioelectronic systems for early detection of kidney transplant rejection. *Science*, 381(6662):1105–1112, 2023.

[45] Mirela Ben-Chen, Craig Gotsman, and Guy Bunin. Conformal Flattening by Curvature Prescription and Metric Scaling. *Computer Graphics Forum*, 27(2):449–458, 2008.

[46] Krzysztof K Dudek, Muamer Kadic, Corentin Coulais, and Katia Bertoldi. Shape morphing metamaterials. *arXiv preprint arXiv:2501.14804*, 2025.

[47] Utpal Nath, Brian C. W. Crawford, Rosemary Carpenter, and Enrico Coen. Genetic Control of Surface Curvature. *Science*, 299(5611):1404–1407, 2003.

[48] Yael Klein, Efi Efrati, and Eran Sharon. Shaping of elastic sheets by prescription of non-euclidean metrics. *Science*, 315(5815):1116–1120, 2007.

[49] Yafei Zhang, Omri Y Cohen, Michael Moshe, and Eran Sharon. Geometrically frustrated rose petals. *Science*, 388(6746):520–524, 2025.

[50] Eric James William Whittaker and Charles Alfred Taylor. *The stereographic projection*. University College Cardiff Press, 1984.

[51] Mina Konaković-Luković, Julian Panetta, Keenan Crane, and Mark Pauly. Rapid deployment of curved surfaces via programmable auxetics. *ACM Trans. Graph.*, 37(4):106:1–106:13, 2018.

[52] Matteo Taffetani, Xin Jiang, Douglas P Holmes, and Dominic Vella. Static bistability of spherical caps. *Proceedings of the Royal Society A: Mathematical, Physical and Engineering Sciences*, 474(2213):20170910, 2018.

[53] Marcus Fairs. Lilium tower in warsaw by zaha hadid, 2008.

[54] Julian Panetta, Florin Isvoranu, Tian Chen, Emmanuel Siéfert, Benoît Roman, and Mark Pauly. Computational inverse design of surface-based inflatables. *ACM Transactions on Graphics*, 40(4):1–14, 2021.

[55] Eitan Richardson and Michael Werman. Efficient classification using the euler characteristic. *Pattern Recognition Letters*, 49:99–106, 2014.

[56] Linas Jonušauskas, Darius Gailevičius, Sima Rekštytė, Tommaso Baldacchini, Saulius Juodkazis, and Mangirdas Malinauskas. Mesoscale laser 3d printing. *Opt. Express*, 27(11):15205–15221, May 2019.

[57] Yoonho Kim, Hyunwoo Yuk, Ruike Zhao, Shawn A. Chester, and Xuanhe Zhao. Printing ferromagnetic domains for untethered fast-transforming soft materials. *Nature*, 558(7709):274–279, 2018.

Acknowledgments

The authors gratefully acknowledge the resource and guidance of the University of Houston Nanofabrication Facility and the Shared Equipment Authority (SEA) at Rice University. Y.W. and T.C. are partially funded by NASA MIRO "Inflatable Deployable Environments and Adaptive Space Systems" (IDEAS2) Center under Grant no. 80NSSC24M0178. Y.S. and T.C. are partially funded by Toyota Research Institute of North America (TRINA).

Author contribution

Y.W., Y.S., and T.C. conceived the study and conducted the numerical work. Y.W. and K.S. conducted the experiments. All authors drafted and revised the manuscript.

Competing Interests

The authors declare no competing interests.